Colloidal liquid crystals in rectangular confinement: Theory and experiment

10 authors, including:

José Alvarado
Massachusetts Institute of Technology
16 PUBLICATIONS **156** CITATIONS

SEE PROFILE

Bela Mulder
FOM Institute AMOLF
135 PUBLICATIONS **3,230** CITATIONS

SEE PROFILE

Pavlik Lettinga
Forschungszentrum Jülich
77 PUBLICATIONS **1,283** CITATIONS

SEE PROFILE

Gijsje H Koenderink
FOM Institute AMOLF
91 PUBLICATIONS **2,646** CITATIONS

SEE PROFILE

Colloidal liquid crystals in rectangular confinement: theory and experiment

Alexander H. Lewis,[a] Ioana Garlea,[b] José Alvarado,[c] Oliver J. Dammone,[d]
Peter D. Howell,[a] Apala Majumdar,[e] Bela M. Mulder,[bf] M. P. Lettinga,[g]
Gijsje H. Koenderink[b] and Dirk G. A. L. Aarts*[d]

We theoretically and experimentally study nematic liquid crystal equilibria within shallow rectangular wells. We model the wells within a two-dimensional Oseen–Frank framework, with strong tangent anchoring, and obtain explicit analytical expressions for the director fields and energies of the 'diagonal' and 'rotated' solutions reported in the literature. These expressions separate the leading-order defect energies from the bulk distortion energy for both families of solutions. The continuum Oseen–Frank study is complemented by a microscopic mean-field approach. We numerically minimize the mean-field functional, including the effects of weak anchoring, variable order and random initial conditions. In particular, these simulations suggest the existence of higher-energy metastable states with internal defects. We compare our theoretical results to experimental director profiles, obtained using two types of filamentous virus particles, wild-type *fd*-virus and a modified stiffer variant (Y21M), which display nematic ordering in rectangular chambers, as found by confocal scanning laser microscopy. We combine our analytical energy expressions with experimentally recorded frequencies of the different equilibrium states to obtain explicit estimates for the extrapolation length, defined to be the ratio of the nematic elastic constant to the anchoring coefficient, of the *fd*-virus.

1 Introduction

Liquid crystals are mesogenic phases of matter with physical properties intermediate between those of the conventional solid and liquid states of matter.[1,2] There are several different types of liquid crystals, of which nematics are the simplest kind. Nematics are complex fluids with long-range orientational order[1,3] and constitute the basis of the multi-billion dollar liquid crystal display industry.[4] Over the past fifty years there has been a constant stream of new technology entering the market, from basic calculator screens to flexible tablet devices. Multistable liquid crystal devices, for which there are several stable nematic equilibria, offer enhanced optical resolution at much reduced power consumption.[5,6] In particular, a bistable liquid crystal display does not need power to support a static image and power is only required to switch between different

images. The promise of bistability has inspired a significant amount of work on novel geometries that induce and support bistability, from arrays of posts to patterned surfaces.[7–9] Recently, shallow nematic-filled square wells have been shown to be bistable, with at least two different stable equilibria: the diagonal and rotated solutions.[10,11] The diagonal and rotated solutions have been studied in subsequent papers,[12–14] with emphasis on both static and dynamic properties. In addition, there is considerable interest in square wells with variable homeotropic and planar anchoring[15–18] for studying systems such as phospholipid interactions.

Motivated by this recent interest, we study nematic equilibria in two-dimensional rectangles of varying aspect ratios, within a continuum Oseen–Frank framework and a microscopic mean-field approach, complemented by parallel experimental studies of confined rod-like viruses in micron-sized shallow rectangular chambers. The modelling assumption of two-dimensional behaviour is a simplification of the 3D behaviour of nematic liquid crystals confined to a shallow cuboid with planar degenerate boundary conditions, and restricts our modelling to consider planar configurations in invariant in the *z*-direction. It is known that non-planar equilibria exist for such systems.[19] However, given that the well depth is much smaller than the well cross-section dimensions, we expect that non-planar equilibria will have significantly higher energies than planar equilibria. A full 3D calculation is possible: one would minimize

[a] *Mathematical Institute, University of Oxford, Oxford, OX2 6GG, UK*

[b] *FOM Institute AMOLF, 1098 XG Amsterdam, The Netherlands*

[c] *Department of Mechanical Engineering, Institute of Technology, 77 Massachusetts Ave., Cambridge, MA 02139, USA*

[d] *Department of Chemistry, Physical and Theoretical Chemistry Laboratory, University of Oxford, Oxford, OX1 3QZ, UK. E-mail: dirk.aarts@chem.ox.ac.uk*

[e] *Department of Mathematical Sciences, University of Bath, Bath, BA2 7AY, UK*

[f] *Laboratory of Cell Biology, Wageningen University, 6708 PB Wageningen, The Netherlands*

[g] *Institut für Festkörperforschung, Forschungszentrum Jülich, 52425 Jülich, Germany*

the (full three-dimensional) free energy with planar degenerate surface anchoring at all six walls, but this lies outside the scope of the current work.

Working within the one-constant approximation for the Oseen–Frank theory and the assumption of tangent anchoring, we compute exact analytical expressions for the diagonal and rotated director profiles and their corresponding energies in terms of the aspect ratio λ and defect core size ε. These solutions were reported experimentally and numerically in several papers[10,12–14] and our results reveal the subtle geometry-dependence of the energies of the equilibria. The mean field approach allows us to capture the effects of variable nematic order and weak surface anchoring, both of which are outside the scope of our analytical Oseen–Frank study. We compute equilibrium states for the mean-field functional using Monte Carlo methods, for different choices of initial conditions, and find three new states with internal defects or uniform alignment. We use laser scanning confocal microscopy with soft-lithography techniques[20–22] to reconstruct the director profiles of rod-like viruses down to the particle level for a range of rectangular wells with different aspect ratios. The experimentally observed profiles include the diagonal and rotated solutions, along with the states predicted by the mean-field approach.

We combine our analytical and experimental results and propose an empirical method to estimate the extrapolation length of the *fd*-virus, defined to be the ratio of the nematic elastic constant to the anchoring coefficient.[23,24] The extrapolation length is a key length-scale for confined nematic systems and measures the relative strengths of elastic and boundary effects. Note that the anchoring strength can be understood as an emergent property of the system, where it is mainly the entropic part of the particle–wall interaction that sets its value, see for example the theoretical work of Dijkstra *et al.* for a hard rod fluid at a wall.[25]

This paper is organized as follows. We review the Oseen–Frank theory and present our analysis in Section 2, followed by the mean-field model and results in Section 3. The experimental methods are described in Section 4. In Section 5, we discuss our results for rod-like viruses and use experiment and theory to derive an explicit estimate for the extrapolation length of the *fd*-virus. We summarize our main results, their implications and possible generalizations in Section 6.

2 Oseen–Frank calculations

The Oseen–Frank theory is the simplest continuum theory for uniaxial nematics, with a single preferred direction of particle alignment and spatially invariant order parameter.[26] It describes the state of the nematic by a unit-vector field, **n**, representing the single distinguished alignment direction, so that all directions orthogonal to **n** are physically equivalent.[2] The directions **n** and −**n** are physically equivalent and hence, **n** is also commonly referred to as the *director field*. The experimentally observed stable states correspond to local or global minima of the Oseen–Frank free energy, $E[\mathbf{n}]$, subject to the imposed boundary conditions.[3,26] The Oseen–Frank free energy density is a quadratic function of the gradient of **n** (see below)

$$E[\mathbf{n}] = \frac{1}{2} \iiint_V \left\{ K_1 (\nabla \cdot \mathbf{n})^2 + K_2 (\mathbf{n} \cdot \nabla \times \mathbf{n})^2 + K_3 (\mathbf{n} \times \nabla \times \mathbf{n})^2 \right\} \mathrm{d}V, \tag{1}$$

where the elastic constants K_1, K_2 and K_3 are associated with characteristic splay, twist and bend director distortions.[1,2]

We define V to be a rectangular well with length X, width Y and depth Z. For shallow wells, we assume that $Z \ll X, Y$ and that the director is invariant in the z-axis. Hence, **n** can be modelled as a two-dimensional unit-vector field and it suffices to restrict attention to the two-dimensional well cross-section,

$$A = \{(x, y) \in \mathbb{R}^2 \colon 0 \leq x \leq X, 0 \leq y \leq Y\}. \tag{2}$$

The energy is invariant under rescaling, so we define $\hat{A}$ to be A rescaled by the length X,

$$\hat{A} = \{(x, y) \in \mathbb{R}^2 \colon 0 \leq x \leq 1, 0 \leq y \leq \lambda\}, \tag{3}$$

where the aspect ratio $\lambda \equiv \dfrac{Y}{X}$. Without loss of generality, we take $\lambda \in (0,1)$.

For analytical purposes, we use the one-constant approximation for which $K_1 = K_2 = K_3 = K$ (ref. 1, 2 and 13) and the Oseen–Frank free energy reduces to

$$E[\mathbf{n}] = \frac{KZ}{2} \iint_{\hat{A}} |\nabla \mathbf{n}|^2 \mathrm{d}A. \tag{4}$$

The unit-vector field, **n**, can be described in terms of an angle θ as shown below

$$\mathbf{n} = \begin{pmatrix} \cos(\theta(x,y)) \\ \sin(\theta(x,y)) \end{pmatrix}, \tag{5}$$

where θ is the angle relative to the x-axis. Under these assumptions, the stable equilibria are minimizers of the Dirichlet energy,[12]

$$E[\theta] = \frac{KZ}{2} \iint_{\hat{A}} |\nabla \theta|^2 \mathrm{d}x\mathrm{d}y, \tag{6}$$

and are solutions of the Laplace equation

$$\nabla^2 \theta = 0, \tag{7}$$

subject to suitable boundary conditions on $\partial \hat{A}$.

We assume strong planar/tangent anchoring on the domain edges *i.e.* surface forces are sufficiently strong so as to induce a fixed orientation parallel to the edges.[1,2] This yields a Dirichlet boundary-value problem for the angle θ defined in (5).

We define a function f which satisfies $\nabla^2 f = 0$, subject to the boundary conditions $f(x, 0; \lambda) = 1$, $f(0, y; \lambda) = f(1, y; \lambda) = f(x, \lambda; \lambda) = 0$. Using the method of separation of variables, we compute f to be

$$f(x, y; \lambda) = \sum_{n=0}^{\infty} \frac{4 \sin((2n+1)\pi x)}{(2n+1)\pi} \left[\cosh((2n+1)\pi y) - \coth((2n+1)\pi\lambda)\sinh((2n+1)\pi y) \right]. \tag{8}$$

By rotating and rescaling the function f, we can express θ as a linear combination of f as shown below:

$$\theta(x,y;\lambda) = a_1 f(x,y;\lambda) + a_2 f\left(\frac{y}{\lambda}, \frac{1-x}{\lambda}; \frac{1}{\lambda}\right) + a_3 f(x, \lambda - y; \lambda)$$
$$+ a_4 f\left(\frac{y}{\lambda}, \frac{x}{\lambda}; \frac{1}{\lambda}\right), \qquad (9)$$

where the coefficients a_i determine the value of θ on the four edges. It is straightforward to verify that any 'tangent' solution of the Laplace equation on a rectangle can be expressed as above.

We impose three constraints on the coefficients a_i in (9): (i) values of a_i are such that $\mathbf{n}$ is parallel to the edges on $\hat{A}$ in sync with the strong tangent anchoring; (ii) there are no interior defects; (iii) and the defects at the four rectangular corners are of strength ± 1, so that θ is locally described by

$$\theta \approx \pm\phi + \text{const}. \qquad (10)$$

near each corner. Any equilibrium state which violates conditions (ii) or (iii) may be observable but is expected to have a higher energy cost compared to equilibria which obey these two conditions.

We then find that all admissible equilibria are equivalent, up to rotation and reflection, to one of three basic solutions in Fig. 1. In the D state, the director aligns along a diagonal line. In the U_1 and U_2 states, the director rotates by π radians between two parallel edges. For $\lambda = 1$, U_1 and U_2 are indistinguishable. These states are generalizations of the diagonal and rotated states identified in a square well.[10,12]

The Dirichlet boundary conditions create discontinuities in θ at the rectangle corners. These correspond to local point defects with logarithmically divergent Oseen–Frank energy.[1,27] We regularize the energy by removing a disc of radius ε around each of the defects, where ε represents the rescaled 'defect core radius'.[2] We take the defect core size to be proportional to the nematic correlation length (see ref. 28 and 29 for definition of correlation length). For two-dimensional systems, the correlation length is the length-scale over which the system relaxes from an ordered nematic state to a disordered isotropic state.

The *regularized* free energy is

$$E_\varepsilon[\theta] = \frac{KZ}{2} \iint_{\hat{A}_\varepsilon} |\nabla\theta|^2 \mathrm{d}x\mathrm{d}y, \qquad (11)$$

where $\hat{A}_\varepsilon$ denotes a rectangle with a quadrant of radius ε removed from each corner, as shown in Fig. 2.

By an application of Green's First Identity,[30] we express $E_\varepsilon[\theta]$ as a line integral about the boundary $\partial\hat{A}_\varepsilon$ with outward pointing normal $\mathbf{n_o}$:

$$E_\varepsilon[\theta] = \frac{KZ}{2} \oint_{\partial\hat{A}_\varepsilon} \theta\nabla\theta \cdot \mathbf{n_o}\mathrm{d}s. \qquad (12)$$

The boundary $\partial A\hat{A}_\varepsilon$ comprises 4 straight edges and 4 circular arcs about the defects, and hence (12) is the sum of 8 line integrals, each of which can be evaluated individually. Using the assumed local behaviour around each corner, we find that the line integrals around the circular arcs are $O(\varepsilon^2)$. The leading-order contributions originate from the line integrals along the straight edges and the regularized energy of the equilibria in Fig. 1 may be expressed as an asymptotic expansion of the form

$$\frac{E_\varepsilon[\theta]}{\pi KZ} \sim \ln\left(\frac{1}{\varepsilon}\right) + \tilde{E}[\theta] + O(\varepsilon^2). \qquad (13)$$

All equilibria have four corner defects of strength ± 1. Hence, the leading logarithmic contribution from the corner defects is the same for all states. The difference in the interior field structure is captured by the *normalized* energy $\tilde{E}[\theta]$, which is independent of ε.

We calculate the normalized energy $\tilde{E}$ explicitly for the three equilibria in Fig. 1:

$$\tilde{E}_D = \ln\left(\frac{2\lambda}{\pi}\right) + s_1\left(\frac{1}{\lambda}\right) - s_2\left(\frac{1}{\lambda}\right), \qquad (14)$$

$$\tilde{E}_{U_1} = \ln\left(\frac{2\lambda}{\pi}\right) + s_1\left(\frac{1}{\lambda}\right) + s_2\left(\frac{1}{\lambda}\right), \qquad (15)$$

$$\tilde{E}_{U_2} = \ln\left(\frac{2}{\pi}\right) + s_1(\lambda) + s_2(\lambda). \qquad (16)$$
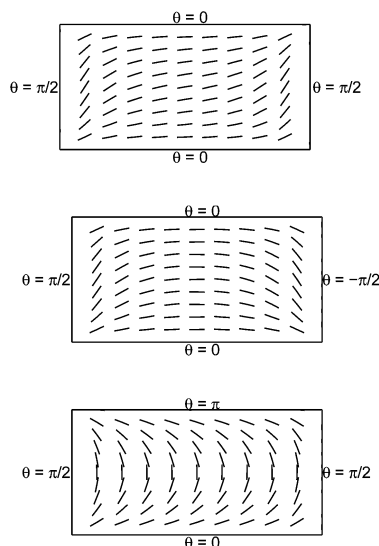

Fig. 1 The diagonal (D) state (top), the rotated (U_1) state (middle) and the rotated (U_2) state (bottom), with sample boundary conditions.
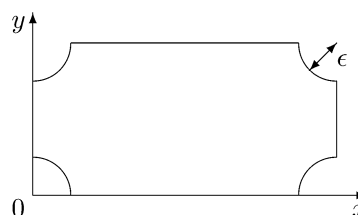

Fig. 2 The domain $\hat{A}_\varepsilon$; the rectangle $\hat{A}$ with quadrants of radius ε removed from each corner.

where the functions s_1 and s_2 are computed to be

$$s_1(\lambda) = 2 \sum_{n=0}^{\infty} \frac{\coth((2n+1)\pi\lambda) - 1}{2n+1}, \qquad (17)$$

$$s_2(\lambda) = 2 \sum_{n=0}^{\infty} \frac{\operatorname{csch}((2n+1)\pi\lambda)}{2n+1}. \qquad (18)$$

Using these expressions, one can easily show that $\tilde{E}_D < \tilde{E}_{U_1} < \tilde{E}_{U_2}$ for all $\lambda < 1$. Hence, the diagonal state always has the minimum energy, while the U_2 state always has the highest energy, as is suggested by the apparent relative deformation of the three director fields depicted in Fig. 1. For $\lambda > 1$, the energy trends of U_1 and U_2 are reversed as expected.

We can readily approximate the functions $s_1(\lambda)$ and $s_2(\lambda)$ asymptotically for small λ, yielding the following estimates for the normalized energy in the limit $\lambda \to 0$:

$$\tilde{E}_D \sim \ln\left(\frac{2\lambda}{\pi}\right) + O\left(e^{-\frac{1}{\lambda}}\right), \qquad (19)$$

$$\tilde{E}_{U_1} \sim \ln\left(\frac{2\lambda}{\pi}\right) + O\left(e^{-\frac{1}{\lambda}}\right), \qquad (20)$$

$$\tilde{E}_{U_2} \sim \frac{\pi}{2\lambda} + \ln\left(\frac{\lambda}{2\pi}\right) + O\left(e^{-\frac{1}{\lambda}}\right). \qquad (21)$$

As $\lambda \to 0$ (with $\varepsilon \ll \lambda$), the energies of the D and U_1 states become exponentially close. This limit corresponds to a very thin rectangle where the y-edge is very short compared to the x-edge, and the energies $\tilde{E}_D$ and $\tilde{E}_{U_1}$ are both dominated by transition layers near the y-edges, within which θ rotates by $\frac{\pi}{2}$ radians from the y-edge to the bulk orientation. The energy of the U_2 state becomes very large in this limit, since the director is constrained to rotate by π radians between a pair of horizontal x-edges. In Fig. 3, we see that the energies of the D and U_1 states asymptotically approach each other as $\lambda \to 0$, while the energy of the U_2 state diverges.
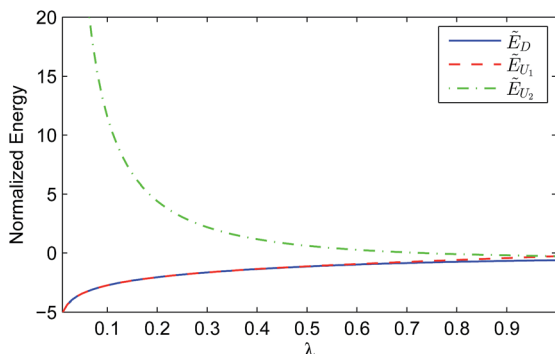

Fig. 3   The normalized energies of the three states plotted against the aspect ratio λ.

3   Mean-field model

The analytical results of the Oseen–Frank theory described in the previous section rely on a number of assumptions. Firstly, the Oseen–Frank theory assumes that the order parameter is constant throughout the sample domain, precluding the spontaneous formation of bulk singularities. Secondly, we assume strong anchoring on the rectangular edges, which fixes θ (and hence **n**) on the edges. One expects that for weaker surface anchorings, the system could relax bulk distortions at the expense of violating the preferred tangent boundary conditions on the edges. To explore these issues, we use a microscopic mean-field theory, designed to be directly comparable to the Oseen–Frank approach in the previous section. As in Section 2, we assume that the system is homogeneous in the z-direction, take the allowed particle orientations to be planar and denote the particle orientations by the 2D unit vector $\hat{\omega} = (\cos\theta, \sin\theta)$.

The generic expression of the appropriate mean-field free energy functional[31] is given by

$$\beta F[\rho^{(1)}] = \iint_A \int_{S^1} d\mathbf{r} d\hat{\omega} \rho^{(1)}(\mathbf{r}, \hat{\omega}) \left\{ \log\left(\mathscr{A}_T \rho^{(1)}(\mathbf{r}, \hat{\omega}) \right) - 1 \right\}$$
$$+ \frac{1}{2} \iint_A \int_{S^1} d\mathbf{r}_1 d\hat{\omega}_1 \iint_A \int_{S^1} d\mathbf{r}_2 d\hat{\omega}_2 \rho^{(1)}(\mathbf{r}_1, \hat{\omega}_1) \rho^{(1)}(\mathbf{r}_2, \hat{\omega}_2)$$
$$\times \mathscr{V}(\mathbf{r}_1, \hat{\omega}_1; \mathbf{r}_2, \hat{\omega}_2) + \beta F_S[\rho^{(1)}(\mathbf{r}, \hat{\omega})]. \qquad (22)$$

Here S^1 is the unit circle in two dimensions, $\rho^{(1)}(\mathbf{r}, \hat{\omega})$ is the one-particle area density as a function of in-plane position $\mathbf{r}$ and particle orientation $\hat{\omega}$, $\mathscr{A}_T \propto \lambda_{\text{Broglie}}^3/Z$ is an otherwise unimportant dimensional factor, $\mathscr{V}(\mathbf{r}_1, \hat{\omega}_1; \mathbf{r}_2, \hat{\omega}_2)$ the (effective) pair-potential and F_S an anchoring free energy.

For the pair-potential, we choose a form that guarantees that the interaction-dependent part of the free-energy is fully characterized by the local 2D tensor order parameter,

$$\mathbf{Q}(\mathbf{r}) = \int_{S^1} d\hat{\omega} \rho^{(1)}(\mathbf{r}, \hat{\omega}) \mathbf{q}(\hat{\omega}) \bigg/ \int_{S^1} d\hat{\omega} \rho^{(1)}(\mathbf{r}, \hat{\omega}), \qquad (23)$$

where $\mathbf{q}(\hat{\omega}) = 2\hat{\omega} \otimes \hat{\omega} - \mathbf{I}_2$ is the second rank molecular orientation tensor. In particular, $|\mathbf{Q}|$ is a measure of the local two-dimensional nematic orientational order.[28] We then write

$$\mathscr{V}(\mathbf{r}_1, \hat{\omega}_1; \mathbf{r}_2, \hat{\omega}_2) = \mathbf{V}^{(0)}(r_1 - r_2) + \mathbf{q}(\hat{\omega}_1) : \mathbf{V}^{(2)}(r_1 - r_2)$$
$$+ \mathbf{V}^{(2)}(r_1 - r_2) : \mathbf{q}(\hat{\omega}_2) + \mathbf{q}(\hat{\omega}_1) : \mathbf{V}^{(4)}(r_1 - r_2) : \mathbf{q}(\hat{\omega}_2), \qquad (24)$$

where : denotes a double contraction. Global rotational invariance constrains the coefficients $\mathbf{V}^{(n)}(\mathbf{r}_1 - \mathbf{r}_2)$ to be the product of a function of the interparticle separation r_{12} and a tensorial expression of order n built from the unit separation vector $\hat{\mathbf{r}} = (\mathbf{r}_1 - \mathbf{r}_2)/r_{12}$ and the identity tensor $\mathbf{I}_2$.[32] We choose the anchoring free energy to be of the form

$$\beta F_S[\rho^{(1)}(\mathbf{r}, \hat{\omega})] = \oint_{\partial A} ds f_S\left(\hat{\mathbf{b}}(\mathbf{r}(s)), \mathbf{Q}(\mathbf{r}(s)) \right), \qquad (25)$$

where the local anchoring energy term is chosen to reproduce the classic Rapini–Papoular expression,[33]

$$f_S\big(\hat{\mathbf{b}}(\mathbf{r}(s)), \mathbf{Q}(\mathbf{r}(s))\big) = \frac{1}{2\sqrt{2}} \frac{W\mathbf{Q}(\mathbf{r}(s)) : \hat{\mathbf{b}}(\mathbf{r}(s)) \otimes \hat{\mathbf{b}}(\mathbf{r}(s))}{\sqrt{\mathbf{Q}(\mathbf{r}(s)) : \mathbf{Q}(\mathbf{r}(s))}} \quad (26)$$

$$= \frac{W}{2}\big(\hat{\mathbf{b}}(\mathbf{r}(s)) \cdot \hat{\mathbf{n}}(\mathbf{r}(s))\big)^2 + \text{const.}, \quad (27)$$

where $\hat{\mathbf{b}}(\mathbf{r})$ is the outward unit normal and $\hat{\mathbf{n}}(\mathbf{r})$ the local director. For $W > 0$, this term favours alignment tangential to the rectangular edges, consistent with the modelling in the previous section.

We assume that the spatial variations of the order parameter, $\mathbf{Q}(\mathbf{r})$, occur on a scale much larger than the range of the interparticle potential and perform a gradient expansion of the nonlocal integrals in the interaction-dependent part of the free energy. This yields an effective free energy of the form

$$\beta F\big[\rho^{(1)}\big] = \iint_A \int_{S^1} \mathrm{d}\mathbf{r}\mathrm{d}\hat{\omega}\rho^{(1)}\big(\mathbf{r}, \hat{\omega}\big)\Big\{\log\big(\mathscr{A}_T\rho^{(1)}\big(\mathbf{r}, \hat{\omega}\big)\big) - 1\Big\}$$
$$- \frac{J}{2}\iint_A \mathrm{d}\mathbf{r}Q_{\mu\nu}(\mathbf{r})Q_{\mu\nu}(\mathbf{r}) + \frac{L_1}{2}\iint_A \mathrm{d}\mathbf{r}\partial_\mu Q_{\nu\tau}(\mathbf{r})\partial_\mu Q_{\nu\tau}(\mathbf{r})$$
$$+ \frac{L_2}{2}\iint_A \mathrm{d}\mathbf{r}\partial_\mu Q_{\mu\nu}(\mathbf{r})\partial_\tau Q_{\tau\nu}(\mathbf{r}) + \frac{L_2}{4}\oint_{\partial A} \mathrm{d}s\hat{b}_\mu(\mathbf{r}(s))$$
$$\times \big\{Q_{\tau\nu}(\mathbf{r}(s))\partial_\tau Q_{\mu\nu}(\mathbf{r}(s)) - Q_{\mu\nu}(\mathbf{r}(s))\partial_\tau Q_{\tau\nu}(\mathbf{r}(s))\big\}$$
$$+ \oint_{\partial A} \mathrm{d}sf_S\Big(\hat{\mathbf{b}}(\mathbf{r}(s)), \mathbf{Q}(\mathbf{r}(s))\Big), \quad (28)$$

where we use the Einstein convention of summing over repeated indices. The mean-field energy (28) has different contributions: a local part involving $\rho^{(1)}$ that constrains the order parameter in the strong interaction limit, a quadratic Landau-de Gennes type bulk component with coupling constant J, elastic energy densities with elastic constants L_1 and L_2 respectively and two surface energy contributions over the boundary ∂A. The standard Frank constants are related to the constants L_i through $K_1 = K_3 \propto L_1 + \dfrac{L_2}{2}$ and $K_2 \propto L_1$.[34] For given values of the coupling parameter J, elastic constants L_1 and L_2 and wall interaction W, we minimize (28) using a simulated annealing Monte Carlo procedure. The details of this procedure, as well as an extended derivation of the free energy, will be published elsewhere.

Results of the numerical minimization procedure are summarized in Fig. 4. For the range of parameters for which boundary and elastic contributions are comparable, we find the two basic patterns discussed in Section 2, the diagonal D pattern and the U_1 pattern. Occasionally, we also find patterns with one or two internal point defects, which we denote by D^* and U_1^* respectively. We find all states for the parameters $J = 1.25$ (such that the order parameter ~ 0.6 in the bulk), $L_1 = 1.25 \times 10^{-5}$, $L_2 = 5 \times 10^{-5}$, and $W = 0.5$. To compare the free energies, we use the system with no elastic coupling (i.e. $L_1 = L_2 = 0$) as a reference, and subtract its free energy from calculated free energies, interpreting the remainder as the effective elastic free energy contribution. In the square geometry, the D state has the minimum elastic free energy. The U_1 pattern has a 20% higher elastic free energy. In the presence of point defects these elastic free energy differences increase even further, the U_1^* configuration with one point
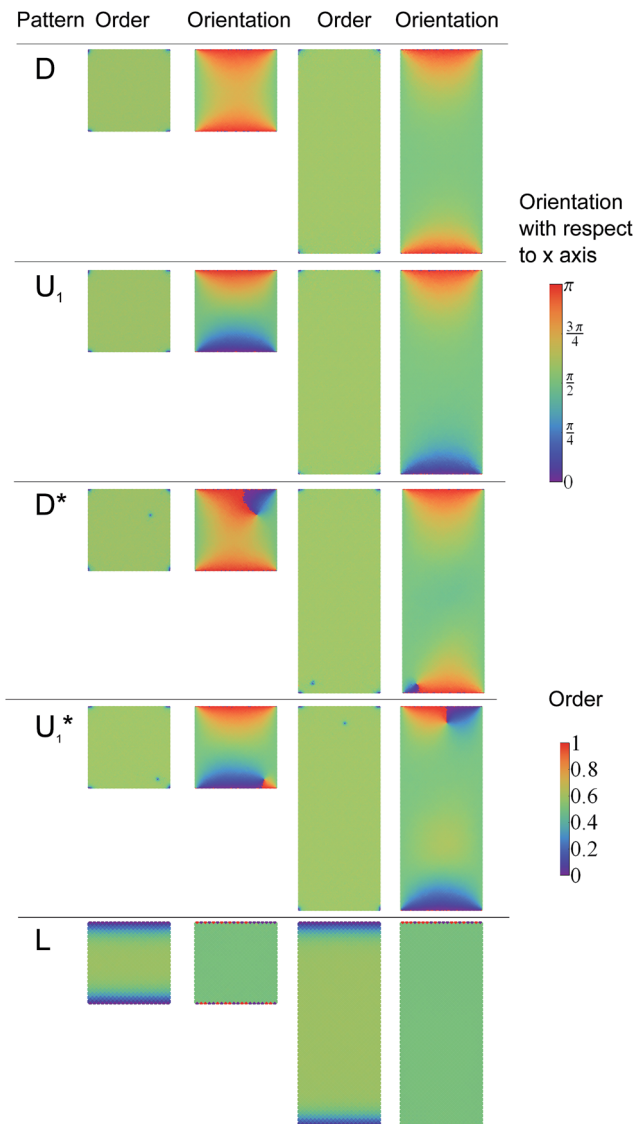

Fig. 4 Representative organization in square and rectangular confinement. The results for all the patterns shown were obtained for $J = 1.25$, $L_1 = 1.25 \times 10^{-5}$, $L_2 = 5 \times 10^{-5}$, and $W = 0.5$.

defect being 23% higher in energy and the D^* state containing two point defects is 40% higher than the D state. In the rectangular geometry, the elastic free energy difference between the D and U_1 states decreases with increasing asymmetry ($\lambda \rightarrow 0$) as the director field will almost everywhere be parallel to the longest wall, effectively decoupling the two end walls, which each impose a free energy cost. Finally, if we increase the elastic constants significantly, the bulk effects dominate the boundary effects and we predict the appearance of the L state, in which the director field is uniform and aligned with the longest axis of the domain. In this case, we find that at the 'misaligned' walls, the system accommodates the mismatch with the boundary potential by significant reduction in the degree of local order.

4 Experimental director fields

To test whether the states predicted by our theoretical models occur experimentally, we confine aqueous suspensions of *fd*-virus to rectangular microchambers. Bulk (unconfined) *fd*-virus suspensions exhibit phase behaviour in agreement with theoretical models of colloidal hard-rod fluids.[35] Here we use two related viruses: the first one is the semi-flexible wild-type (WT) *fd*-virus and the second one is a variant virus known as Y21M, which has a single mutation of the major coat protein that causes a 3-fold increase of the stiffness.[36] Both viruses consist of a single strand of DNA wrapped in a helical coat of *ca.* 2700 copies of the major coat protein pVIII.[35] Both viruses have a contour length of 0.88 μm and a diameter of 6.6 nm. We study suspensions at concentrations of 18 and 24 mg ml^{-1} for the WT *fd*-virus, and of 13 and 20 mg ml^{-1} for the Y21M variant, as determined by UV-vis spectrophotometry. These concentrations are just below and above the isotropic–nematic biphasic region respectively. We choose the lowest possible nematic concentration, as we expect that this minimizes the free energy penalty for rearrangement of the director fields and therefore reduces the probability of ending up in high energy metastable states. We choose the highest isotropic concentration, to check whether confinement can lead to a capillary-induced nematic phase.

Fluorescently labelled rods (labelled with Alexa488 succinimidyl ester) are mixed at a small volume fraction (2–4%) with unlabelled rods, to act as tracers to reveal the director field. The fluorescently labelled viruses are imaged using confocal microscopy. High spatial resolution images are obtained using a Nikon C1 confocal microscope, while time-resolved imaging is carried out using a Leica inverted microscope with a Yokogama CSU22 spinning disk unit. For spinning disc measurements, ten movies of 200 frames each are acquired per condition at a fast imaging rate (0.1 frames per second), which are separated by 2 minutes each to allow the rods to diffuse across the chamber. For point-scanning confocal data, ∼15–30 frames are acquired at a slower rate (1 frame per ∼1–2 minutes) over several fields of view, which are automatically acquired and stitched (NIS Elements, Nikon).

Standard soft lithography techniques are used to create chips containing several hundred separate rectangular microchambers made of the negative photoresist material SU8 (SU8-2005, MicroChem).[21,22] The rectangles have short edges with a length Y ranging from 2 to 50 μm, and aspect ratios $\lambda = Y/X$ ranging from 0.0545 to 1. The chamber depth is fixed between 0.7 and 3 μm, which is sufficiently shallow to create quasi-2D confinement, since the cholesteric pitch is almost 2 orders of magnitude larger than the depth.[37] Additionally, 3D *z*-scans confirm the absence of cholesteric twist, that is normally present in bulk nematic phases of *fd*-viruses.

The chips are plasma-cleaned for 1 minute to make the microchamber surfaces clean and hydrophilic, before the filling procedure. The chips are filled by pipetting a drop of the sample onto the chip and the droplet spreads out due to the chips' hydrophilicity. This results in slightly different filling conditions for each cell; however, we do not observe any noticeable effect of the filling conditions on the nematic director. The chambers are hermetically sealed with a microscope slide coated with a layer of polydimethylsiloxane (PDMS) passivated with Pluronic F-127 (Sigma-Aldrich).

5 Experimental results and extrapolation length

We observe the samples *ca.* 20 minutes after filling the chambers. During this time interval, the particles spontaneously align into various distinct ordered steady-state patterns, as summarised in Fig. 5. The system is strongly confined in the *z*-direction. Confocal scans at different heights do not show any *z*-
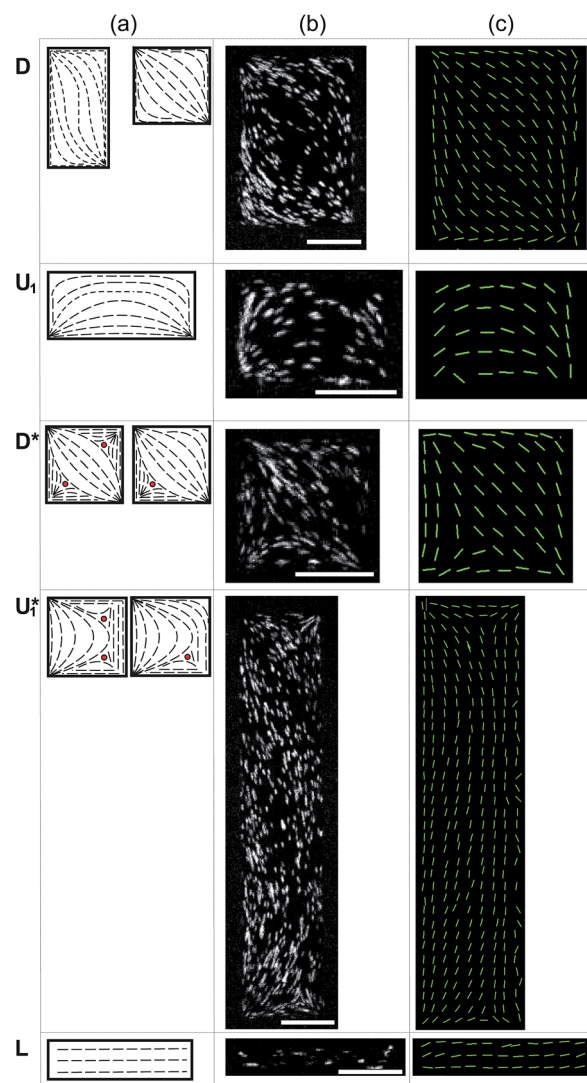

Fig. 5 Examples of the director fields observed in rectangular cells for WT *fd* and Y21M. (a) Sketch of the director field. Internal defects are indicated by red circles. (b) Four overlaid spinning disk confocal images, with scale bar = 10 μm. (c) Experimental director field calculated from a series of 1000 images. Of the examples given, the D and L states are WT *fd* and U$_1$, U$_1^*$ and D* states are Y21M.

dependence and the rods show planar alignment at the top and bottom walls. Experimentally, there is no observation of a preferred orientation of the rods on the bottom or top wall, indicating degenerate planar anchoring conditions. The director fields are observed over a 24 hour period, during which no switching occurs. This is indicative of high energy barriers between the states. In total, we observe 290 chambers containing Y21M rods and 57 chambers containing WT fd-rods. In Fig. 6, we show the phase space in terms of chamber dimensions, λ and Y.

We experimentally find all the states predicted in Sections 2 and 3, with the exception of the U_2 state. Most frequently occurring is the energy minimizing D state, followed by the slightly higher energy U_1 state (Fig. 6). The D^* and U_1^* states share the basic structure of the D and U_1 states, with one or two internal defects of strength $-\frac{1}{2}$. These states occur infrequently, consistent with the increased energy cost associated with extra

defects. The L state, characterised by all the rods lying tangent to the longest side, only occurs for small values of both Y and λ. We note that the experimental director fields compare favourably with theoretical structures.

In recent work, some of us have shown that the WT fd-virus has elastic constants $K_3 \approx K_1$,[20] but for the Y21M virus, $K_3 \gg K_1$ $\left(\frac{K_3}{K_1} \approx 20\right)$.[38] This implies that the theoretical work in Section 2 can only be directly applied to the WT fd-virus. However, the qualitative director profiles are similar for both viruses and a full theoretical analysis of the elastically anisotropic Y21M virus will be given elsewhere.

The L state occurs with the same frequency as the D and U_1 states for particular values of Y and λ. The corresponding chamber dimensions for equal observational frequencies can be directly measured from our experiments (see Table 1). We assume that the L state and the D/U_1 states have equal energies whenever they have equal observational frequency. Strictly speaking, this is only valid when the different configurations can be seen to switch between states on the experimental timescale.[39] This switching is not observed here, as mentioned above. Instead, we assume that the frequency with which states are sampled from their initial random configuration is a measure of their energy and use this to estimate the extrapolation length for the fd-virus as shown below.

For the L state, the director is approximately uniform along the long rectangular edge and hence the elastic energy vanishes. However, the tangent boundary conditions are violated along the shorter edges. We include the Rapini–Papoular anchoring described in (27), which for constant order parameter simplifies to

$$E_S[\theta] = \oint_{\partial A} \frac{W}{2} \sin^2(\theta - \theta_0)\mathrm{d}s, \tag{29}$$

where W is the anchoring strength and θ_0 is the direction of preferred alignment. The L state then has energy

$$E_L = YZW. \tag{30}$$

For equal observational frequencies of D/U_1 and L, we equate the asymptotic expression for the regularized energy for the D/U_1 states with the anchoring energy for the L state above and obtain an estimate for the extrapolation length of the fd-virus below,

$$\xi = \frac{K}{W} \approx \frac{Y}{\pi \ln\left(\frac{2Y}{\pi\hat{\varepsilon}}\right)}, \tag{31}$$
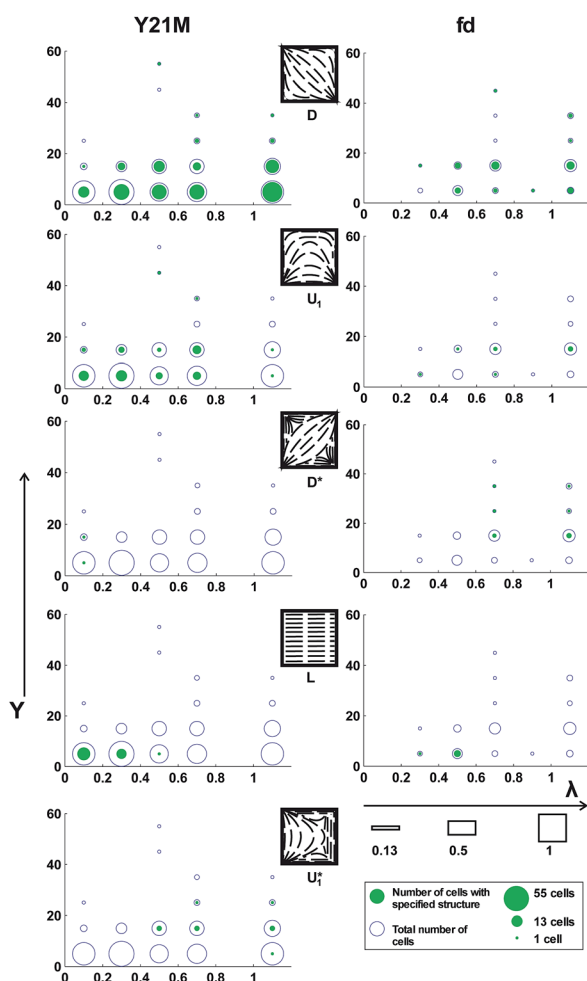

Fig. 6 Phase space for rectangular cells. We plot the length of the shortest side, Y, versus the aspect ratio, λ, for the director fields shown in Fig. 5. The circle area is proportional to the number of cells. The area of the filled circles is proportional to states exhibiting the specified director field. The left hand column contains results for Y21M and the right hand column for WT fd-virus.

Table 1 The values of Y and λ when the frequencies of the D and U_1 states coincide with the frequencies of the L state for the WT fd-virus and the associated estimate of the extrapolation length. Values of Y and λ were derived by interpolating between observed frequencies

State	Y (μm)	λ	ξ (μm)
D	6.8	0.4	1.4
U_1	7.4	0.5	1.4

in terms of Y and the defect core radius $\hat{\varepsilon}$. We assume that $\hat{\varepsilon}$ is similar to the length of the virus, 0.88 μm, as can be inferred from the experimental images in Fig. 5.

We then find that the extrapolation length, ξ, is of the order of particle length (see Table 1). Our estimate compares favourably with a previously reported theoretical estimate of ξ for the *fd*-virus,[40] as well as other rod-like colloidal liquid crystal systems such as carbon nanotubes[41] and vanadium pentoxide,[42,43] and colloidal platelets.[44–46]

6 Conclusions

In this paper, we have investigated nematic equilibria in shallow micron-scale rectangular wells with tangent boundary conditions. We model the wells within a continuum Oseen–Frank framework and a mean-field framework separately. In the Oseen–Frank case, we obtain explicit analytical expressions for the diagonal and rotated solution profiles and the corresponding energies. The energy estimates clearly separate the defect energies from the energy cost of bulk distortion within the rectangular domain. These analytical estimates are of independent interest and the methods may be adapted to other two-dimensional domains.

The microscopic mean-field approach allows us to include the effects of surface anchoring and variable order parameter. We find three further states, denoted D^*, U_1^* and L. We use a two-dimensional model wherein defects necessarily correspond to isotropic regions. We would expect the defects to have an intricate biaxial structure[47,48] within a three-dimensional Landau-de Gennes model. This is outside the scope of the two-dimensional methods employed in this paper.

We perform parallel experiments on rod-like viruses in micron-scale rectangular chambers. We find examples of all the theoretically predicted states, with the exception of the high energy U_2 state. Finally, we obtain an estimate for the extrapolation length of the *fd*-virus by combining our analytical energy estimates (in the Oseen–Frank framework) with experimental observations. Such methods can be generalized to systems with elastic anisotropy such as Y21M and provide an alternative method for obtaining estimates of the extrapolation length for both thermotropic and lyotropic liquid crystalline systems.

References

1 P. G. de Gennes and J. Prost, *The Physics of Liquid Crystals*, Oxford University Press, 2nd edn, 1998.

2 I. Stewart, *The Static and Dynamic Continuum Theory of Liquid Crystals: A Mathematical Introduction*, Taylor & Francis, 2004.

3 N. Mottram and C. Newton, *Introduction to Q-tensor Theory*, University of Strathclyde technical report, 2004.

4 D. Dunmur and T. Sluckin, *Soap, Science and Flat-Srcreen TVs: A History of Liquid Crystals*, Oxford University Press, 2010.

5 N. A. Clark and S. T. Lagerwall, *Appl. Phys. Lett.*, 1980, **36**, 899.

6 D. W. Berreman and W. R. Heffner, *J. Appl. Phys.*, 1981, **52**, 3032–3039.

7 B. W. Lee and N. A. Clark, *Science*, 2001, **291**, 2576–2580.

8 J.-H. Kim, M. Yoneya and H. Yokoyama, *Nature*, 2002, **420**, 159–162.

9 S. Kitson and A. Geisow, *Appl. Phys. Lett.*, 2002, **80**, 3635–3637.

10 C. Tsakonas, A. J. Davidson, C. V. Brown and N. Mottram, *Appl. Phys. Lett.*, 2007, **90**, 111913.

11 Y. Yi, M. Nakata, A. R. Martin and N. A. Clark, *Appl. Phys. Lett.*, 2007, **90**, 163510–163510.

12 C. Luo, A. Majumdar and R. Erban, *Phys. Rev. E: Stat., Nonlinear, Soft Matter Phys.*, 2012, **85**, 061702.

13 A. J. Davidson and N. J. Mottram, *Eur. J. Appl. Math.*, 2012, **23**, 99–119.

14 J. Chen, *Soft Matter*, 2013, **9**, 10921–10930.

15 M. K. McCamley, G. P. Crawford, M. Ravnik, S. Žumer, A. W. Artenstein and S. M. Opal, *Appl. Phys. Lett.*, 2007, **91**, 141916.

16 M. K. McCamley, M. Ravnik, A. W. Artenstein, S. M. Opal, S. Žumer and G. P. Crawford, *J. Appl. Phys.*, 2009, **105**, 123504.

17 J. M. Brake, M. K. Daschner and N. L. Abbott, *Langmuir*, 2005, **21**, 2218–2228.

18 V. K. Gupta and N. L. Abbott, *Science*, 1997, **276**, 1533–1536.

19 A. Majumdar, J. M. Robbins and M. Zyskin, *J. Phys. A: Math. Gen.*, 2004, **37**, L573.

20 O. J. Dammone, I. Zacharoudiou, R. P. A. Dullens, J. M. Yeomans, M. P. Lettinga and D. G. A. L. Aarts, *Phys. Rev. Lett.*, 2012, **109**, 108303.

21 M. S. e Silva, J. Alvarado, J. Nguyen, N. Georgoulia, B. M. Mulder and G. H. Koenderink, *Soft Matter*, 2011, **7**, 10631–10641.

22 J. Alvarado, B. M. Mulder and G. H. Koenderink, *Soft Matter*, 2014, **10**, 2354–2364.

23 M. P. Allen, *Mol. Phys.*, 1999, **96**, 1391–1397.

24 A. M. Ribas, L. R. Evangelista, A. J. Palangana and E. A. Oliveira, *Phys. Rev. E: Stat., Nonlinear, Soft Matter Phys.*, 1995, **51**, R5204.

25 M. Dijkstra, R. v. Roij and R. Evans, *Phys. Rev. E: Stat., Nonlinear, Soft Matter Phys.*, 2001, **63**, 051703.

26 A. Majumdar and A. Zarnescu, *Arch. Ration. Mech. Anal.*, 2010, **196**, 227–280.

27 M. Klemen, *Rep. Prog. Phys.*, 1989, **52**, 555–654.

28 A. Majumdar, *Comm. Pure. Appl. Anal.*, 2012, **11**, 1303–1337.

29 S. Mkaddem and E. Gartland, Jr, *Phys. Rev. E: Stat., Nonlinear, Soft Matter Phys.*, 2000, **62**, 6694.

30 A. E. Danese, *Advanced Calculus*, 1965, **vol. 1**.

31 C. Zannoni, in *The Molecular Physics of Liquid Crystals*, ed. G. W. G. G. R. Luckhurst, Academic Press, 1979, ch. 3, pp. 51 – 83.

32 C. Rosenblatt and D. Ronis, *Phys. Rev. A*, 1981, **23**, 305–315.

33 A. Rapini and A. Papoular, *J. Phys., Colloq.*, 1969, **30**, 54–56.

34 P. Sheng and E. B. Priestly, in *Introduction to Liquid Crystals*, ed. E. B. Priestly and P. J. Wojtowicz, Springer, US, 1976, ch. 10, pp. 143–201.

35 Z. Dogic and S. Fraden, *Curr. Opin. Colloid Interface Sci.*, 2006, **11**, 47–55.

36 E. Barry, D. Beller and Z. Dogic, *Soft Matter*, 2009, **5**, 2563–2570.

37 Z. Dogic and S. Fraden, *Langmuir*, 2000, **16**, 7820–7824.

38 O. J. Dammone, *PhD Thesis*, University College, University of Oxford, 2013.

39 T. L. Hill, *An Introduction to Statistical Thermodynamics*, Courier Dover Publications, 1960.

40 P. Prinsen and P. van der Schoot, *Phys. Rev. E: Stat., Nonlinear, Soft Matter Phys.*, 2003, **68**, 021701.

41 N. Puech, E. Grelet, P. Poulin, C. Blanc and P. Van Der Schoot, *Phys. Rev. E: Stat., Nonlinear, Soft Matter Phys.*, 2010, **82**, 020702.

42 P. Prinsen and P. van der Schoot, *Eur. Phys. J. E*, 2004, **13**, 35–41.

43 A. Kaznacheev, M. Bogdanov and S. Taraskin, *J. Exp. Theor. Phys.*, 2002, **95**, 57–63.

44 A. Verhoeff, I. Bakelaar, R. Otten, P. van der Schoot and H. Lekkerkerker, *Langmuir*, 2010, **27**, 116–125.

45 D. van der Beek, H. Reich, P. van der Schoot, M. Dijkstra, T. Schilling, R. Vink, M. Schmidt, R. van Roij and H. Lekkerkerker, *Phys. Rev. Lett.*, 2006, **97**, 087801.

46 A. Verhoeff, R. Otten, P. van der Schoot and H. Lekkerkerker, *J. Chem. Phys.*, 2011, **134**, 044904.

47 S. Kralj and A. Majumdar, *Proc. R. Soc. A*, 2014, **470**, 20140276.

48 N. Schopohl and T. J. Sluckin, *Phys. Rev. Lett.*, 1987, **59**, 2582–2584.